Research Article | Vol. 28, No. 9 / 27 April 2020 / Optics Express 13497
Optics EXPRESS

Tunable narrow band optical reflector based on indirectly coupled micro ring resonators

ALI EMRE KAPLAN,[1,2,*] PAOLO BASSI,[2] AND GAETANO BELLANCA[1]

[1]Department of Engineering, University of Ferrara, Via Saragat, 1, Ferrara 44122, Italy
[2]Department of Electrical, Electronic and Information Engineering, University of Bologna, Viale del Risorgimento, 2, Bologna 40136, Italy
[*]aliemre.kaplan@unife.it

Abstract: This paper presents a novel narrow band wavelength selective optical reflector implemented by indirectly coupling two micro ring resonators in silicon-on-insulator technology. The device is studied using an analytical model based on the transfer matrix method. With the proposed configuration, by electrically driving the integrated micro heaters, a single reflection wavelength with narrow bandwidth can be tuned. The experimental results show a good agreement with the model outcomes. The average measured reflectivity over a wavelength span of 37 nm is 0.55, with a peak of about 50 pm full-width-half-maximum, which corresponds to a quality factor of ~30, 000. The proposed device can offer an alternative approach to realize compact reflective structures for single wavelength reflection operations in photonic integrated circuits.

1. Introduction

Optical ring resonators have been first proposed by Marcatili in 1969, to investigate propagation losses in waveguide bends [1]. They are attracting and versatile components, particularly suitable for many applications ranging from wavelength channel filters [2–4] to laser cavities [5,6], modulators [7], routers or switches [8–11]. Ring resonators can be fabricated with different integration technologies. In the recent years, high index contrast integration platforms made the fabrication of small footprint photonic devices possible; among them silicon-on-insulator (SOI) technology [12], attracting for its compatibility with CMOS devices, is of particular interest.

In this paper we propose the use of micro ring resonators (MRRs) for the realization of tunable integrated mirrors with good performance: single wavelength, high reflectivity, large free spectral range (FSR) and narrow bandwidth. Mirrors realized by MRRs have been previously proposed in literature for various applications such as laser cavities and sensing, as well as reflective filters in wavelength division multiplexing (WDM) systems [13–25]. Resonator-based reflectors can be implemented by using many different configurations. For example, devices based on two rings [18,19,21] or three and even more rings [20] have been proposed. A major drawback of these solutions is that they exhibit multiple reflected wavelengths, spaced according to the device overall FSR. Increasing the FSR to obtain a single working wavelength requires a reduction of the MRR radius, with an immediate fallout in an unacceptable increase of bending loss attenuation. To tackle this issue, cascaded ring resonators have been proposed to enhance the FSR and pass band flatness without suffering from the reduced radius [26–28] issues (see [29] for more examples). Coupled resonators could benefit of the vernier effect, which increases the wavelength tuning range (e.g. as end mirrors in laser applications [17,24,30]). Other approaches for realizing single wavelength reflectors combine a Y-branch splitter with an embedded microring/microdisk [16,23] or sidewall Bragg grating assisted ring and racetrack resonators [22,25]. The main problem with these approaches, though interesting results have been recently presented [31], is related to the footprint: indeed, a very high number of periods is needed to guarantee high reflection. Moreover, precise fabrication of these gratings requires a high quality lithography process.

#389830 https://doi.org/10.1364/OE.389830
Journal © 2020 Received 5 Feb 2020; revised 20 Mar 2020; accepted 31 Mar 2020; published 20 Apr 2020

Optics EXPRESS

Previously reported double ring based reflectors use directly coupled rings. They exhibit reflections in presence of resonance mode splitting induced by coupling between the clockwise (CW) and counter clockwise (CCW) propagation modes. However, mode splitting for wavelength reflection occurs only in specific coupling conditions, especially when coupling between cavities is weak [19]. This requires an additional design effort to precisely determine the cavity-to-cavity coupling coefficients. Moreover, fabrication issues such as sidewall roughness, which may produce strong reflections that propagate back to input port [32], can harshly influence the performance of the device.

In this work, to get rid of the mentioned problems, we propose a different approach to realize optical reflectors. The structure consists of two crossed waveguides with two rings placed behind the cross and mutually coupled through the central bus waveguide, as shown in Fig. 1. When the rings resonate at the same wavelength, the light propagating from the input port is coupled to the two rings and then driven toward the respective drop ports. However, due to the coupling with the other ring in the drop path (which resonates at the same wavelength), the light is driven back to the input port, thus giving rise to the desired reflection. In this case, the only condition for the reflection to take place is the existence of a common resonance for the two rings. This requirement can be satisfied by manufacturing rings with the same radius or, for the case of rings with different radii, through thermal tuning using integrated micro heaters. For our structure, coupling between rings and waveguides can only influence the performance of the device, but is not at the base of the reflection mechanism, which only depends on the phase shift difference induced on light propagation by the two rings. All the other paths for the traveling light, in fact, are shared. When the phase mismatch is zero or an integer number of 2π, i.e. when the two rings are synchronous for a specific wavelength, reflection occurs and the structure operates as a mirror (Fig. 1(a)). On the contrary, if the rings are not synchronous (Fig. 1(b)), the device behaves as a router. Although this application is interesting, it is outside the scope of this work, which will be therefore focused on the mirror function it allows.

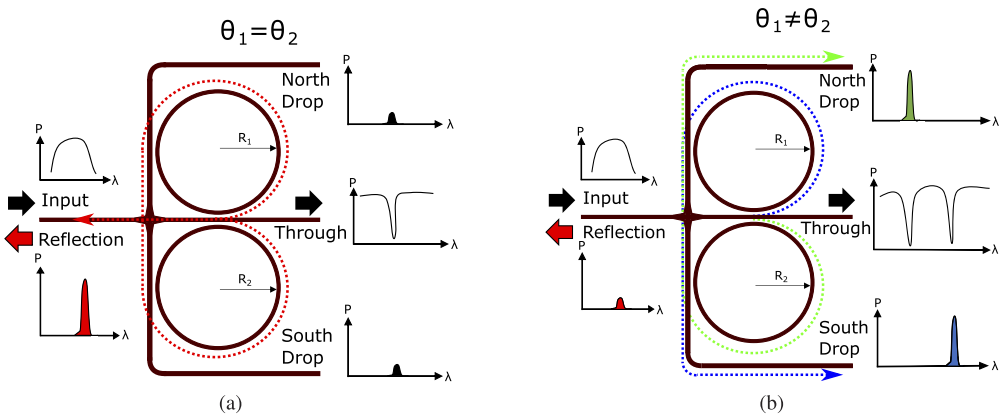

Fig. 1. Working principle of the device when used (a) as a reflector, in the case of phase shift synchronization ($\theta_1 = \theta_2$ at the common resonance of the two rings), and (b) as a router, when $\theta_1 \neq \theta_2$ for all the ring resonances.

Besides its versatility, the device is attracting also for its simplicity. The preliminary design work concerning the coupler sections requires only the optimization of bend-to-waveguide coupling for maximizing the performance. This ease the use of the standard Process Design Kits (PDKs) for single MRRs, available in any fabrication facility. In fact, MRRs are one of the well-known basic building blocks among the photonic integrated circuits. Consequently, once the single ring resonator parameters are known, designing the whole device is straightforward.

Optics EXPRESS

The paper is organized as follows. In the next section, the device's working principle and the analytical model based on transfer matrices are introduced. The design parameters maximizing the reflection are also addressed. In Section 3, we show the experimental results obtained from the fabricated device and briefly describe the details of the fabrication. The spectral behavior for different tuning conditions are presented and discussed. Finally, conclusion remarks about the device performance are provided.

2. Working principle and theoretical background

Figure 1 illustrates the two previously introduced different working regimes supported by the investigated device. The resonators are fed by the input port placed in the left hand side. Unlike the other implementations of ring-based reflectors, where two cavities are directly coupled, the configuration presented in this work has indirectly coupled rings. In fact, they are coupled to each other through a central bus waveguide. The strength of the field coupled to each cavity depends on both the waveguide-to-bend separation and on the radii of the resonators (R_1 and R_2). The coupling varies according to the wavelength. The resonant wavelengths are dropped by the rings and driven to the respective output ports. However, when the rings are synchronized the light is readdressed back to the input port, thus giving rise to reflection (as shown by the dotted-red path in Fig. 1(a)). In this case the rings have, at the wavelength corresponding to the shared resonance, the same optical lengths. This implies $\theta_1 = \theta_2$, being $\theta_1 = n_{eff1}L_1$ and $\theta_2 = n_{eff2}L_2$, where n_{eff_i} and L_i are the effective refractive index of the mode and the circumference of each ring, respectively. Once the phase shift synchronization condition at a specific wavelength is fulfilled, the transmitted powers at the drop and at the through ports vanish and the back reflection to the input port reaches the maximum intensity (Fig. 1(a)). This is the configuration of interest for the application of this device as a reflector.

For the resonances where the synchronization condition is not fulfilled, routing to the drop ports takes place. In this case, in fact, the rings have different optical lengths, that implies $\theta_1 \neq \theta_2$. The top and bottom drop ports therefore receive different wavelengths, reversely routed by the resonators as shown in Fig. 1(b).

The phase shift synchronization can be obtained by fabricating rings with the same radii or, in case of different rings, through thermo-optical tuning. In the former case, all the resonances are synchronized and a comb-type reflected spectrum, i.e. a spectrum where many peaks are present, results. Reflected wavelengths are spaced depending on the FSR of the rings, with peaks not equally spaced due to effective index dispersion. In the latter case, two close resonances can be superimposed by shifting one to coincide with the other, and a single reflected wavelength is then obtained. Thermal tuning can also be used to shift the operating wavelength of the device by heating both rings, in order to adjust the reflected wavelength to the desired value, or to reconfigure it as a router avoiding any superimposition of the resonances, as it will be explained in the next section of the paper.

To investigate the behavior of the proposed device, an analytical model based on the transfer matrix method has been implemented. This method uses, as input quantities, the propagation parameters of the waveguide mode such as the group index (n_g) and the effective refractive index obtained from a Finite Element Method (FEM) solver [33]. The bend-to-straight waveguide coupling parameter, on the contrary, has been calculated through Finite Difference Time Domain (FDTD) simulations [34]. For the sake of simplicity, we assume that all the components except the rings are lossless. The crossing is also crosstalk free. This is a reasonable assumption, since present fabrication standards guarantee a very low crosstalk for this component [35]. Moreover, crosstalk is not fundamental for the reflection to take place, and can only possibly influence the final performance of the device. In the analytical model, we also neglect the stochastic backscatterings that may occur due to the sidewall roughness in the straight waveguides and bends. These simplifications, though important, do not significantly alter the overall behavior of

Optics EXPRESS

the device and allow the development of a model which is extremely useful in determining the role of the different parameters on the device behavior, when used as a reflector.

2.1. Transmission matrix equations

The schematic of the device, as well as the quantities necessary to describe how it works, are illustrated in Fig. 2. The incident (E_{in}) and outgoing (E_{p2}, E_{p3}, E_{p4}) complex mode amplitudes are grouped according to their propagation direction. The couplers with two waveguides (DC_1 and DC_2) are in vertical direction, while the three waveguide coupler (DC_3) is placed horizontally. In the schematic, the propagation direction of the positive superscript sign amplitudes is represented with red arrows, while the negative ones are green colored.

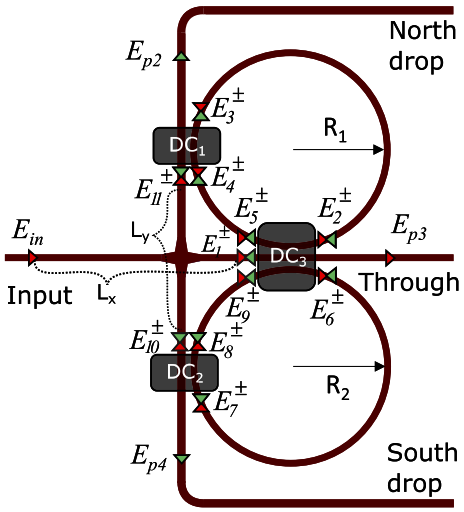

Fig. 2. Schematic of the indirectly coupled resonator with indication of the mode amplitudes. Red colored arrows represent the positive sign mode amplitudes while the green ones depict those of negative signs.

Table 1 lists the design parameters that are used in the model. Starting by setting $E_{in} = 1$, the power transmissions at the output ports are normalized. As previously stated, the straight waveguides are assumed to be lossless ($\alpha_{wg} = 1$). This does not limit the validity of the results, since waveguide propagation loss contributes only to the overall insertion loss of the device. In the vertical direction, E_{p2} and E_{p4} are the field amplitudes at the drop ports connected by the crossing. The distance between them, L_y, which is also the distance between the two vertical couplers, depends on the radius of the rings. The phase shift between the ports of the vertical couplers DC_1 and DC_2 can be defined as $e^{i\theta_y} = e^{i\beta_{wg}L_y}$, where the propagation constant $\beta_{wg} = 2\pi n_{eff}/\lambda$. Similarly, the central input (E_1^+) of DC_3 can be written as $E_1^+ = e^{i\theta_x}E_{in}$, where the phase shift between the input port and DC_3 is defined as $e^{i\theta_x} = e^{i\beta_{wg}L_x}$, and L_x is the length of the input waveguide measured from the excitation port.

The coupling matrices of the two-waveguide couplers DC_1 and DC_2 can be therefore defined as [36–38]

$$\begin{bmatrix} E_{p2} \\ E_3^- \end{bmatrix} = \begin{bmatrix} \cos(\kappa_1 L_{c_1}) & -i\cdot\sin(\kappa_1 L_{c_1}) \\ -i\cdot\sin(\kappa_1 L_{c_1}) & \cos(\kappa_1 L_{c_1}) \end{bmatrix} \begin{bmatrix} E_{11}^+ \\ E_4^- \end{bmatrix} \tag{1}$$

$$\begin{bmatrix} E_{p4} \\ E_7^- \end{bmatrix} = \begin{bmatrix} \cos(\kappa_2 L_{c_2}) & -i\cdot\sin(\kappa_2 L_{c_2}) \\ -i\cdot\sin(\kappa_2 L_{c_2}) & \cos(\kappa_2 L_{c_2}) \end{bmatrix} \begin{bmatrix} E_{10}^- \\ E_8^- \end{bmatrix} \tag{2}$$

Optics EXPRESS

Table 1. Design parameters

Parameter	North ring	South ring	Waveguides
Radius	R_1	R_2	–
Loss coefficient	α_1	α_2	α_{wg}
Propagation constant	β_1	β_2	β_{wg}
Phase shift per round trip	θ_1	θ_2	–
Phase shift in horizontal wg section	–	–	θ_x
Phase shift in vertical wg section	–	–	θ_y
Coupler length of DC1	L_{c_1}	–	–
Coupler length of DC2	–	L_{c_2}	–
Coupler length of DC3	–	–	L_{c_3}
Coupling coefficient of DC1	κ_1	–	–
Coupling coefficient of DC2	–	κ_2	–
Coupling coefficient of DC3	–	–	κ_3

and

$$\begin{bmatrix} E_{11}^- \\ E_4^+ \end{bmatrix} = \begin{bmatrix} \cos(\kappa_1 L_{c_1}) & -i\cdot\sin(\kappa_1 L_{c_1}) \\ -i\cdot\sin(\kappa_1 L_{c_1}) & \cos(\kappa_1 L_{c_1}) \end{bmatrix} \begin{bmatrix} 0 \\ E_3^+ \end{bmatrix} \tag{3}$$

$$\begin{bmatrix} E_{10}^+ \\ E_8^+ \end{bmatrix} = \begin{bmatrix} \cos(\kappa_2 L_{c_2}) & -i\cdot\sin(\kappa_2 L_{c_2}) \\ -i\cdot\sin(\kappa_2 L_{c_2}) & \cos(\kappa_2 L_{c_2}) \end{bmatrix} \begin{bmatrix} 0 \\ E_7^+ \end{bmatrix}. \tag{4}$$

Furthermore, the coupling matrices of the three-waveguide coupler DC_3 can be defined as [39]

$$\begin{bmatrix} E_2^+ \\ E_{p3} \\ E_6^+ \end{bmatrix} = \begin{bmatrix} c_1+0.5 & c_2 & c_1-0.5 \\ c_2 & 2c_1 & c_2 \\ c_1-0.5 & c_2 & c_1+0.5 \end{bmatrix} \begin{bmatrix} E_5^+ \\ E_1^+ \\ E_9^+ \end{bmatrix} \tag{5}$$

$$\begin{bmatrix} E_5^- \\ E_1^- \\ E_9^- \end{bmatrix} = \begin{bmatrix} c_1+0.5 & c_2 & c_1-0.5 \\ c_2 & 2c_1 & c_2 \\ c_1-0.5 & c_2 & c_1+0.5 \end{bmatrix} \begin{bmatrix} E_2^- \\ 0 \\ E_6^- \end{bmatrix} \tag{6}$$

where $c_1 = \frac{1}{2}\cos(\sqrt{2}\kappa_3 L_{c_3})$ and $c_2 = \frac{-i}{\sqrt{2}}\sin(\sqrt{2}\kappa_3 L_{c_3})$. Since only the forward propagation excited from the input port is considered, the zeros in right hand side matrices have the meaning of non existing propagation from the output ports to the input one.

By solving the above matrices, the final explicit expressions of the drop ports (E_{p2}, E_{p4}) can be found as (see Appendix for a full derivation)

$$E_{p2} = \frac{-i\cdot\sin(\kappa_2 L_{c_2}) e^{i3\theta_2/4}\alpha_2^{3/4} e^{i\theta_x} e^{i\theta_y}[Ac_2(B_1 + B_2 M_1^- \sin(k_1 L_{c_1})\sin(\kappa_2 L_{c_2})) + B_1 c_2 M_2^+]}{A\cos(\kappa_1 L_{c_1})} \tag{7}$$

Optics EXPRESS

$$E_{p4} = \frac{-i \cdot \sin(\kappa_1 L_{c_1}) e^{i3\theta_1/4} \alpha_1^{3/4} e^{i\theta_x} e^{i\theta_y} [Ac_2(B_1 + B_2 M_1^- \sin(\kappa_1 L_{c_1}) \sin(\kappa_2 L_{c_1})) + B_1 c_2 M_2^+]}{A \cos(\kappa_2 L_{c_2})} \quad (8)$$

along with the through port (E_{p3})

$$E_{p3} = \frac{2c_1 A + c_2^2 [B_2 \cos(\kappa_1 L_{c_1}) e^{i\theta_1} \alpha_1 + B_1 \cos(\kappa_2 L_{c_2}) e^{i\theta_2} \alpha_2]}{A} \quad (9)$$

and finally the reflection (E_1^-)

$$E_1^- = \frac{-c_2^2 \sin(\kappa_1 L_{c_1}) \sin(\kappa_2 L_{c_2}) e^{i3\theta_1/4} e^{i3\theta_2/4} e^{i\theta_x} e^{i\theta_y} B_1 B_2 (\alpha_1^{3/4} + \alpha_2^{3/4})}{A^2} \quad (10)$$

where $B_{(1,2)} = 1 - M_{(1,2)}^+ + M_{(1,2)}^-$ and $A = (1 - M_1^+)(1 - M_2^+) - M_1^- M_2^-$ letting $M_{(1,2)}^\pm = (c_{(1,2)} \pm 0.5) \cos(\kappa_{(1,2)} L_{c_{(1,2)}}) e^{i\theta_{(1,2)}} \alpha_{(1,2)}$.

To better highlight the behavior of the device, lossless rings with different radii have been initially considered. As anticipated, depending on the phase condition at the resonance, two different transmission schemes are possible, as shown in Fig. 3 and Fig. 4. Figure 3 refers to the situation in which there are no common resonances for the rings (asynchronous case), while Fig. 4 is for the synchronous case, where at least a common resonance exists.

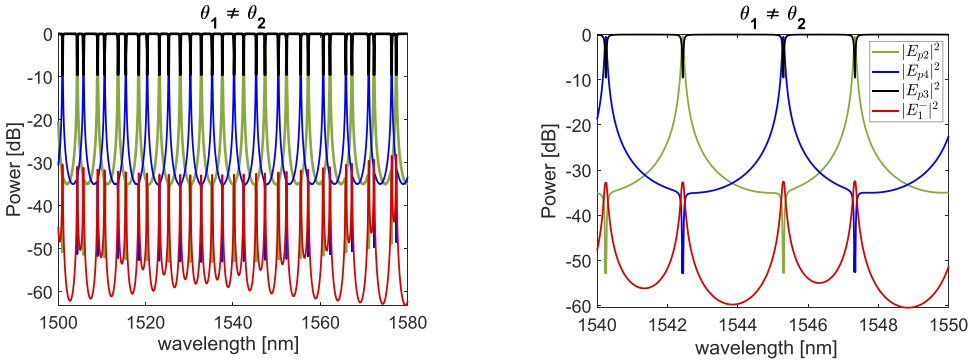

Fig. 3. (a) Theoretical transmission spectra of reflection (Red), through (Black), North drop (Green) and South drop (Blue) ports, when all the resonances in the spectrum are in the asynchronous case ($\theta_1 \neq \theta_2$); (b) enlarged view in the central region of the spectrum.

In the asynchronous case, all the resonances of the two rings are different, and the power reflected back to the input port is negligible. As seen from Fig. 3(b), the reflected powers at the resonances are determined by the drop port Extinction Ratio (ER). In fact, for each resonance the only contribution to the reflection comes from the power re-routed toward the input port by the off resonant ring, and it is proportional to the ratio between the power at the through port and the power at the drop. This power re-routing toward the input port is also responsible for the transmission dips observed in the drop spectra.

When the two rings resonate at the same wavelength ($\lambda \simeq 1547$ nm in Fig. 4), i.e. in the synchronous case, the reflection reaches its maximum value. As one can notice, this is observed only for the wavelength corresponding to degenerate resonance modes. For non-degenerate resonant modes, i.e. for asynchronous resonances, the same behavior previously described can be observed. Close resonances show reflection peaks too, but not as high as the one observed when

Optics EXPRESS

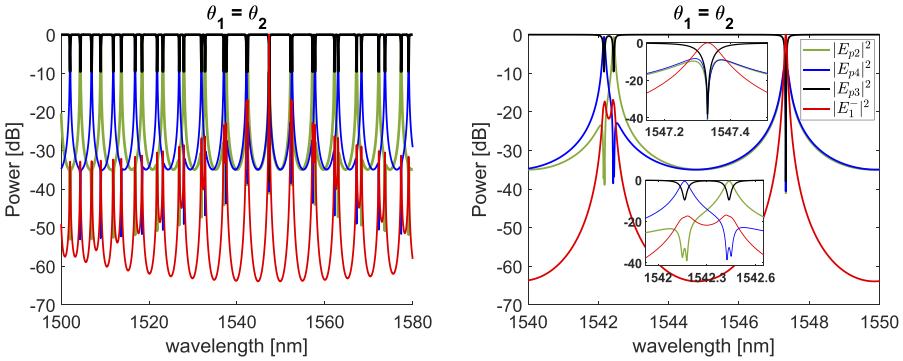

Fig. 4. (a) Theoretical transmission spectra of reflection (Red), through (Black), North drop (Green) and South drop (Blue) ports, when a synchronous resonance exists ($\theta_1 = \theta_2$ for $\lambda \simeq 1547$ nm); (b) enlarged view with insets of the transmission curves for this resonance (top plot) and (bottom plot) for two asynchronous resonances.

the resonances of the two rings are synchronous. The side mode reflections, i.e. the reflections at non-degenerate resonances, have double peak profiles due to the proximity of the two different resonances with suppression (defined as the difference between the maximum intensity of the main peak and the maximum intensity of the strongest minor peak) below -15 dB.

The presence of a high reflection for the synchronous resonance has a direct impact also on the through and drop port transmissions, as it can be observed in the top inset of Fig. 4(b). Indeed, both through and drop ports have high transmission rejection in a very narrow band. The depth of these dips is related to the critical coupling condition. If the critical coupling condition is fulfilled, in fact, the device acts as an optical isolator with respect to the output ports and totally reflects the incoming light back to the input, as it will be discussed in the next section.

2.2. Critical coupling

The critical coupling is a required condition to achieve the highest ER of the through port (E_{p3}) transmission. The transmitted power at this port at the resonance, in fact, can theoretically be canceled. This depends on the balancing among the power coupled to the ring, the power coupled back by the ring to the waveguides and the power lost in the resonators. In a single ring device, the critical coupling condition is present at the resonance when the propagation losses in the ring are compensated by the power coupled into it, if the coupler is assumed to be lossless [40]. In the double ring structure proposed in this paper, if the rings have the same radii and the same coupling with the waveguides, they are synchronized in terms of round trip phase shift and new parameters can be replaced as it follows

$$\begin{aligned} \alpha_1 &= \alpha_2 = \alpha \\ \theta_1 &= \theta_2 = \theta \\ \kappa_1 &= \kappa_2 = \kappa_v \\ \kappa_3 &= \kappa_h. \end{aligned} \tag{11}$$

Here, we define new coefficients κ_v and κ_h as the vertical and horizontal coupling coefficients and the analysis mainly investigates their ratio. To make coupling strengths more significant in the solutions, they can be redefined as $\kappa_h^{'} = \kappa_3 L_{c_3}$ and $\kappa_v^{'} = \kappa_v L_{c_1} = \kappa_v L_{c_2}$. By substituting the

Optics EXPRESS

new parameters from (11) into (9), one can get the through port transmission function

$$E_{p3} = \frac{2c_1A + 2Bc_2^2\cos(\kappa_v^{'})e^{i\theta}\alpha}{A}. \tag{12}$$

Since the cavities are identical, A and B can be written as $A = (1 - M^{+})(1 - M^{+}) - (M^{-})^2 = (1 - M^{+} - M^{-})(1 - M^{+} + M^{-})$ and $B_{1,2} = (1 - M^{+} + M^{-})$ where $M_1^{\pm} = M_2^{\pm} = M^{\pm}$. Finally, the simplified expression of the through port transmission can be obtained as

$$E_{p3} = \frac{\cos(\sqrt{2}\kappa_h^{'}) - \cos(\kappa_v^{'})e^{i\theta}\alpha}{1 - \cos(\sqrt{2}\kappa_h^{'})\cos(\kappa_v^{'})e^{i\theta}\alpha}, \tag{13}$$

and the corresponding power can be written in the form

$$P_{p3} = |E_{p3}|^2 = \left|\frac{\cos(\sqrt{2}\kappa_h^{'}) - \cos(\kappa_v^{'})e^{i\theta}\alpha}{1 - \cos(\sqrt{2}\kappa_h^{'})\cos(\kappa_v^{'})e^{i\theta}\alpha}\right|^2. \tag{14}$$

When the rings are on resonance, $\theta = 2\pi m$ and $m = 1, 2, 3\cdots$, the critical coupling condition is found to be

$$\alpha = \frac{\cos(\sqrt{2}\kappa_h^{'})}{\cos(\kappa_v^{'})}. \tag{15}$$

As Eq. (15) shows, the critical condition holds when the internal cavity loss is equal to the power coupling ratio of the horizontal and vertical couplers. If the rings are lossless ($\alpha = 1$), the critical coupling ratio becomes $\kappa_v^{'} = \sqrt{2}\kappa_h^{'}$, which allows to define the ratio between the power coefficients in the form $K_h = K_v/2$. As a result of this condition, critical coupling is achieved when the horizontal power coupling is half of the vertical one. It must be pointed out that this condition reduces to the well known $K_h = K_v$ for the case of single micro ring resonator [41]. On the other side, in lossy cases (α<1) the critical coupling condition is met by specific values of $\kappa_h^{'}$ and $\kappa_v^{'}$. From the design point of view, this means a need of optimization of either horizontal or vertical couplers according to the value of α, since the relationship between α and the ratio $\kappa_h^{'}/\kappa_v^{'}$ defines the device performance in terms of ER of the through port and of IL of the drop port transmissions at the resonance.

2.3. Loss and coupling ratio analysis for the device performance

In this section, we investigate how the cavity radiation losses and the coupling coefficients of the horizontal and vertical couplers affect the transmission and the reflection characteristics of the proposed device. The critical coupling condition for the double ring resonator is defined by Eq. (15). When this condition is verified, and rings are synchronous, the transmission is minimized and the reflection is maximized. However, examining how the device performs when this condition is not fulfilled can be useful to understand the role of the different parameters on the device behavior. The effects of the cavity radiation losses and of the power coupling ratio K_h/K_v on the reflection and on the transmission at the through and drop ports are illustrated in Fig. 5. In this analysis, K_h/K_v varies from 0.1 up to 2. The figure has two rows: the top line shows the results of the synchronous case ($\theta_1 = \theta_2$), for the wavelength of the peak of Fig. 4(b) near $\lambda = 1547$ nm. The figures on the bottom lines, on the contrary, refer to the asynchronous case ($\theta_1 \neq \theta_2$) and results for the resonant peak near $\lambda = 1545$ nm of Fig. 3(b) are reported. Transmissions and reflections are all plotted in dB.

From the left side column plots it can be noticed that, regardless the phase shift conditions, there are certain cases where the ER reaches −45 dB. On the other hand, the drop port transmission reduces by around -9 dB when the two rings are in phase at the common resonant wavelength.

Optics EXPRESS

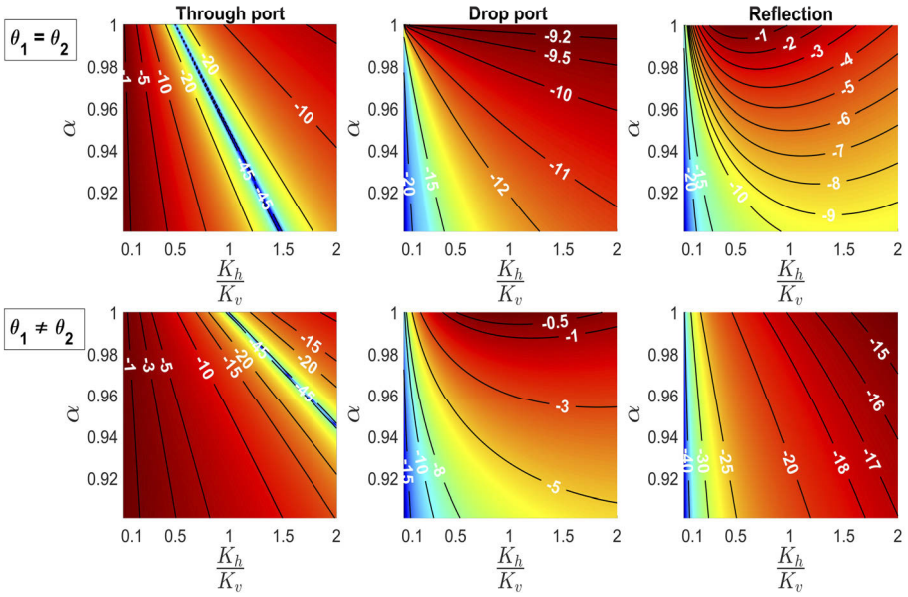

Fig. 5. Relationships between the loss coefficient (α) and the power coupling ratio K_h/K_v of the horizontal and vertical couplers on the transmissions of the through port (left column), drop ports (middle column) and Reflection (right column). The upper row plots are for the synchronous case ($\theta_1 = \theta_2$) and refer to the common resonant wavelength $\lambda \simeq 1547$ nm, while the bottom row charts show the results for the asynchronous case ($\theta_1 \neq \theta_2$) when $\lambda \simeq 1545$ nm.

As shown in the right column plots, the highest value of the reflection, which is theoretically 0 dB, can only be achieved for the synchronous case (top row of Fig. 5) when the rings are lossless ($\alpha = 1$) and the horizontal coupling is half of the vertical coupling ($K_h/K_v = 0.5$). In the asynchronous case (bottom row of Fig. 5), the reflected light intensity at the resonance does not exceed -15 dB. For both cases, the reflection is very sensitive to ring losses, as it rapidly decreases when raising the attenuation inside the resonators.

These results demonstrate that the device can be configured to exhibit, at a synchronous resonance, optical isolation at the transmission ports. In this case, in fact, the only outgoing field is the reflected one. Once the loss coefficient of the resonators is known, the coupling coefficients of DC_1, DC_2, and DC_3 can be designed accordingly. For instance, if $\alpha = 0.995$, in order to achieve a reflection > -1 dB (equivalent to a reflectivity of 0.794), the ratio K_h/K_v must lie between 0.4 and 0.75.

3. Experimental results

A microscope image of the narrow band optical reflector is shown in Fig. 6(a). The device has been fabricated on SOI technology. The layer stack of the structure is illustrated in Fig. 6(b). The gold made metal pads and wide electric connections are used to apply the voltage to the titanium metal heaters placed above the resonators. The resistance of each electrode is 14 Ω and depends mainly by the length of the titanium strip covering the ring. Focusing grating couplers are used to transfer the light between the fibers and the device. Coupling losses are of the order of 5 dB. The deep etched SOI waveguide of Fig. 6(b) has 480 nm width and 220 nm height and supports single quasi-TE mode in the operation wavelength span. The ring-to-waveguide separation (gap) in both vertical and horizontal coupling sections is 150 nm; rings radii are $R_1 = 18$ μm and $R_2 = 19$ μm. As rings are different, the synchronous resonances at the desired wavelength must be configured

Optics EXPRESS

by thermal tuning. During this operation, because of the proximity of the rings, thermal crosstalk is possible and an undesired drift of the resonance could be observed. To overcome these effects, approaches such as thermal crosstalk cancellation described in [42] should be applied.

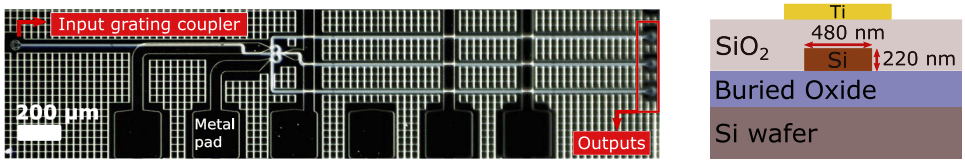

(a) (b)

Fig. 6. (a) Microscope image of the fabricated reflectors with metal deposition for micro heaters and probe pads; (b) cross section of the single quasi-TE mode SOI waveguide with the titanium heater on top.

The transfer function of the transmissions and reflections have been obtained with an optical tester, fed by a tunable laser. The reflection spectrum is retrieved from the input port using a circulator. In this way, the input and reflected signals can be independently measured. The integrated heaters used for resonance tuning are driven by a suitable power supply. Figure 7 shows the wavelength shift according to the power applied to the resistor on the ring. The calculated tuning efficiency obtained from the slope of the linear fit was found to be 115 pm/mW. The resonators have FSR of 5.04 and 4.76 nm for the radii of 18 and 19 μm, respectively. Therefore, the maximum required power to tune the reflected wavelength within the FSR is below 45 mW.

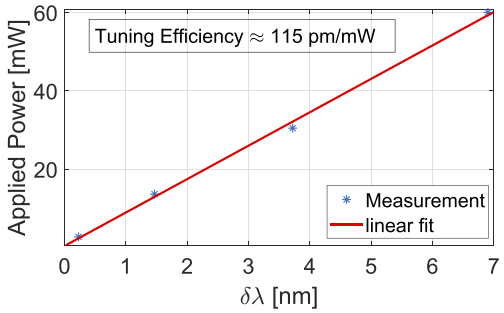

Fig. 7. Measured resonance wavelength shift with respect to the applied power.

The experimental results of the drop and through ports when the electrodes are not polarized are shown in Fig. 8(a). In the following, we will refer to this configuration as the OFF state. When no voltage is applied to the electrodes, all the resonances are phase-unmatched and separated in the considered wavelength range. As shown in Fig. 8(b), the two dropped wavelengths near 1540 and 1542 nm have $Q = 17,500$ and 10 GHz of bandwidth. The North and South drop ports both show weaker secondary resonance wavelength peaks driven by the other ring. This is caused by backscattered signals induced by the sidewall roughness of the waveguides, which are not considered in the analytical model. These signals, in fact, induce counter propagating modes which appear in the spectrum of each drop. Such resonances occur at the wavelengths where the model predicts coupling effects between the rings. Without backscattering, such effects would be a further decrease of the signal at the drop output. With backscattering, on the contrary, some undesired signal is present in the channel. It however adds in spectral positions where the signal level is much lower, being then less harmful for the device performance. As said before, differently from the previously reported configurations based on side-by-side coupled double

Optics EXPRESS

rings, the coupling of these modes is not required for the reflection condition. Our device in fact, thanks to its topology, performs reflections using mutually shared light paths for re-routing the dropped wavelengths back to the input port.

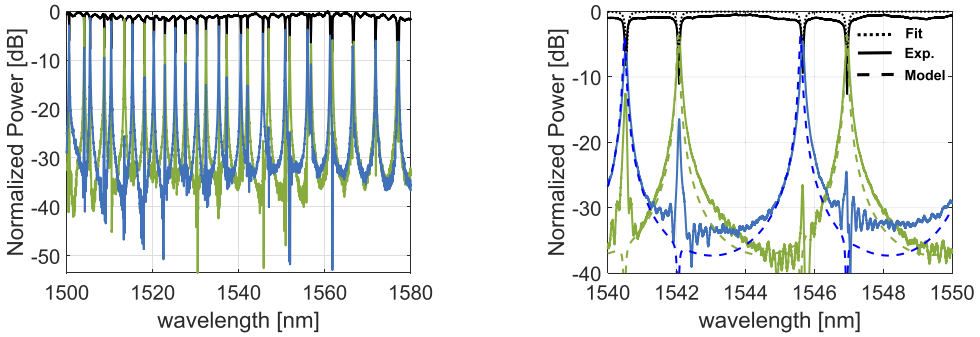

Fig. 8. (a) Measured transmission spectra of through (Black), North drop (Green) and South drop (Blue) ports in the OFF state (no applied voltage to the electrodes); (b) enlarged view in the 1540 ÷ 1550 nm wavelength range. In this figure, the dotted Black curve is the fit, with the analytical model, of the through port. In the same plot, the calculated drop outputs are also illustrated (dashed curves). In this situation, all the resonances in the considered portion of the spectrum are asynchronous, and therefore separated.

In order to compare the model outputs with the experimental results, we first extracted the technological parameters, such as group index, coupling and loss coefficients, by fitting our model to the measurements in the OFF state. The fitting plot of the through port is the dotted Black curve of Fig. 8(b). The parameters extracted from this fit are reported in Table 2. The fitted loss coefficients α_1 and α_2 are in good agreement with the expected propagation losses in the cavity, considering 3 dB/cm waveguide loss. The curves of the North (dashed Green) and South (dashed Blue) drop ports obtained through the transfer matrix model using the parameters obtained from the fitting are also plotted in Fig. 8(b). The same fitted parameters have been also used in the analytical model to reproduce device responses when the resonators are synchronized (ON state) for the common resonance. In this case, thermally induced effective index change is reintroduced in the model.

Table 2. The extracted parameters obtained by fitting the parameters of the model with experimental results.

ng	$\partial n_{eff}/\partial\lambda$	R_1	R_2	k_1	k_2	k_3	α_1	α_2
4.08	$1.046{\cdot}10^6$	18.02	19.01	0.232	0.236	0.033	0.986	0.987

To configure the device as a reflector, i.e. to turn it from the OFF to the ON state, 1.7 V have been applied to the electrodes of the North ring. This causes a shift of 1.7 nm on the peak of E_{p4}, which now superimposes to the peak of E_{p2} for $\lambda \simeq 1547$ nm. The power required for this shift is about 14 mW. As seen in Fig. 9(b), in this situation the power of the dropped wavelength is reduced to about -10 dB and the power reduction compared to the OFF state is close to 5 dB. Furthermore, the ER of E_{p3} increased up to 22 dB, with a difference of ΔER = 11 dB with respect to the non synchronized case.

The measured spectra of E_1^- (reflection) and E_{p3} (through) are shown in Fig. 10(a). When the rings are tuned to have a common resonance at $\lambda \simeq 1547$ nm, a very narrow band reflection peak ($Q \approx 30,000$) with 50 pm (6.4 GHz) of linewidth and 11 dB of ER becomes maximized at the resonance ($\lambda \simeq 1547$ nm). The measured reflection to transmission ratio is found to be

Optics EXPRESS

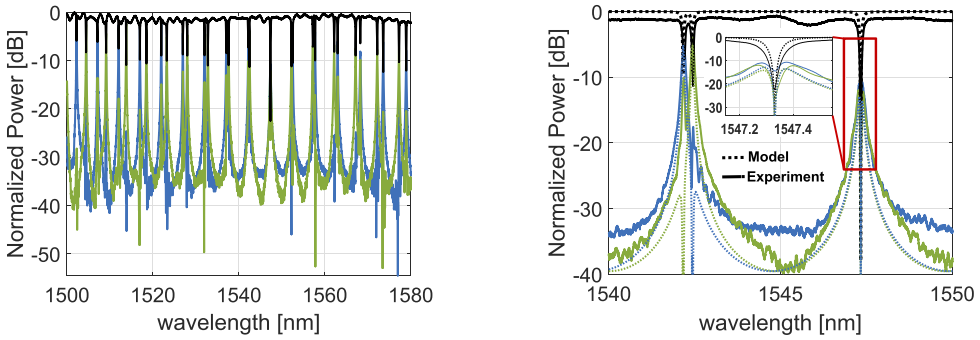

Fig. 9. (a) Measured transmission spectra of through (Black), North drop (Green) and South drop (Blue) ports with an applied voltage of 1.7 V to the North ring; (b) enlarged view in the 1540 ÷ 1550 nm wavelength range. As it can be noticed, the phase synchronization is present for $\lambda \simeq 1547$ nm.

0.96 (linear scale). As seen in Fig. 10(b), a secondary peak 9.87 nm on the right from the main resonance appears. This secondary peak has an intensity 2 dB below the intensity of the main peak. This undesired peak occurs because of the proximity of two non-degenerate resonant modes. The suppression of side modes gets higher when resonances are more separated in wavelength. We also found from the model results that reflection port suppression depends on Q-factor: the higher the Q factor, the higher the side mode suppression.

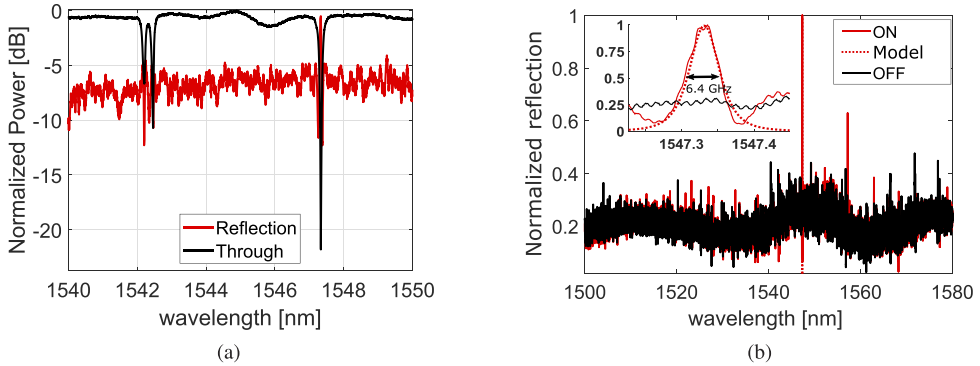

Fig. 10. Transmission and reflection as a function of the wavelength when the device is in the ON state (a). Comparison of the measured reflection spectra in the OFF (Black curve) and ON (Red curve) states (b). The enlarged view shows the spectra in the region of the peak comparing also measurements with simulated results (Red dotted curve) for $\lambda \simeq 1547$ nm.

Evaluation of the actual reflectivity by comparing the ratio between reflected and the transmitted signals is not straightforward. In fact, thermal tuning for phase alignment is sensitive to measurement errors and the maximum reflection is achievable in a very small wavelength range. Moreover, other contributions to the reflection such as fiber to waveguide coupling, backscattering and Fabry-Pérot oscillations between input and output gratings, result in a reflection floor distributed over the spectrum even in the OFF state, as shown in Fig. 10(b). Since the measurements of ON and OFF states can have different reflection floors, we calculated the reflectivity by measuring the reflection enhancement with respect to the floor level at the

Optics EXPRESS

wavelength of the resonance. As a result, each reflection peak is investigated with its own reflection floor and the difference is considered as the actual reflectivity coefficient.

The reflector has been tested in the wavelength range of 1520 - 1560 nm by applying suitable polarization voltages to the integrated heaters in order to tune the reflection, i.e. in order to superimpose two ring resonances, at the desired wavelength. Figure 11 shows the measured reflectivity over a span of 37 nm. The maximum measured value is found to be 0.63 (linear scale), similar to the predicted value of 0.68 obtained from the model using the fitted parameters. The measured reflectivity has an average value of 0.55 in the considered wavelength span and the maximum oscillation of about 15%. The change in the measured reflectivity, which was not foreseen in the analytical model, is due to the dependence on the wavelength of the coupling coefficients of the couplers. Since the horizontal and the vertical couplers are different, their ratio changes when tuning the device and therefore also the reflectivity, as shown in the reflection plot of Fig. 5.

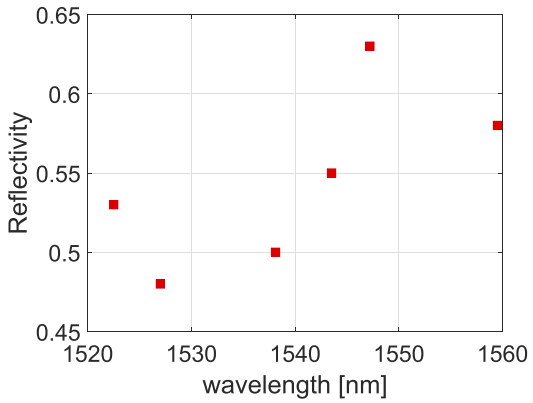

Fig. 11. Measured reflectivity as a function of the wavelength obtained through thermal-tuning.

In order to have a uniform reflections in the tested wavelength range, the difference between the cavity lengths should be reduced. However, in this case, the identical radii will increase the strength of the side mode reflections and eventually lead to a periodic comb reflection spectrum, since more resonances could be simultaneously phase synchronized. Using different radii, such as 18 and 19 μm, allows to restrict the number of simultaneous resonances to a single one at a fixed wavelength.

As stated earlier, higher reflectivity and side mode suppression require low losses in the cavity. According to simulations, a propagation loss of 1 dB/cm in the rings, neglecting the bend loss, would be sufficient to achieve a reflectivity higher than 0.9 and to improve side mode suppression up to 10 dB.

Wavelength dependence of other important quantities such as ER and FWHM of the reflection peaks are shown in Fig. 12(a). The linewidth of reflected resonances varies from 40 to 52 pm while the ER range is between 6.65 and 11 dB. Since the propagation losses in bend sections can be minimized by increasing the radius, the preliminary study on the coupling coefficient takes an important role for the critical coupling condition to achieve narrow linewidth reflection spectra.

Figure 12(b) shows the measured ER in the ON state (synchronous rings at the resonance) and its increase ΔER compared with respect to the OFF state (asynchronous rings at the resonance). The maximum observed ER is near a wavelength of 1560 nm, where ΔER = 29 dB. From this plot it is possible to observe that, even though the reflection condition requires a high ER in through port transmission, reflectivity strength and ER can be uncorrelated. In fact, as it can be noticed from the plots in the first row of Fig. 5, there is no correspondence between high reflection and

Optics EXPRESS

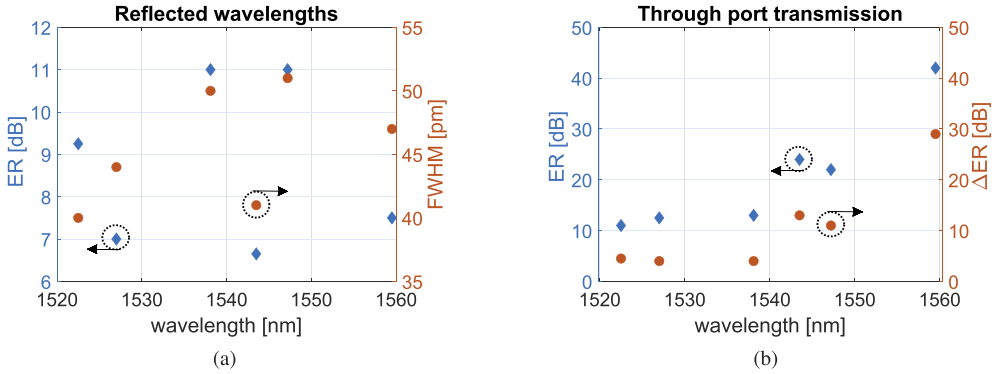

Fig. 12. (a) Measured ER and FWHM of the reflected peaks as a function of the wavelength while tuning the common resonance of the two rings through the heaters; (b) measured ER of the through port transmissions with its enhancement ΔER compared to OFF state.

high ER. Moreover, regardless the phase matching condition is satisfied (bottom row in the same figure), the through port always presents a high ER region depending on the coupling ratio of the horizontal and vertical couplers. As an example, by considering the asynchronous case ($\theta_1 \neq \theta_2$) with the values of $K_h/K_v = 2$ and a loss coefficient $\alpha \approx 0.95$, it is still possible to obtain the highest ER achievable and keep the reflection power to less than -15 dB.

Comparisons among previously reported ring based reflectors [21–25] and the device proposed in this work are shown in Table 3. Only the experimental works are included in the list. While the grating assisted resonators show higher reflectivity [22,25] our device, together with the reflector in [23], produces much narrower reflection bandwidth. Unfortunately, the results reported in [23] do not provide the reflectivity value. That device is a different implementation of the one originally fabricated in Polymer [16] (not in the list because of lack of information on both reflectivity and FWHM), where the ring is substituted by a microdisk. The reflectors in [21] and [24] are made by two rings that are side by side coupled to each other. While the former was fabricated in Polymer, the latter was made of silicon and used as an external cavity to realize a tunable laser. As said before, the working principle of these mirrors is based on counter propagating modes coupling. The devices presented in [23] and [25] combine a resonator with two Y-branch splitters that connect the input and output ports to implement Mach-Zehnder interferometer, where the branches of such interferometer are coupled to a resonator as in add/drop configuration.

Table 3. Comparison of experimental demonstrations of ring based reflectors

Reference	Device Type	Material	Reflectivity	FWHM (pm)
[21]	Directly coupled double MRRs[b]	Polymer	0.23	120
[22]	Grating assisted single MRR[a]	Si_3N_4	0.92	400
[23]	Single microdisk resonator[a]	Silicon	N/A	17
[24]	Directly coupled double MRRs[b]	Silicon	0.7[c]	160
[25]	Grating assisted racetrack resonator[a]	Silicon	0.74[d]	147
This work	Indirectly coupled double MRRs[b]	Silicon	0.63	51

[a]not tunable,
[b]tunable,
[c]estimated,
[d]simulated

Optics EXPRESS

All reflectors listed in Table 3 use MRRs in either all-pass or add/drop configurations while our device uses a grid configuration, with two perpendicular waveguides connected through a crossing waveguide. MRRs in grid configuration offer compact and scalable wavelength switching matrices and the indirectly coupled resonators in such configuration can benefit from its single wavelength reflective property. Note that the device is also scalable, in the sense that, to realize a multi-wavelength reflector, devices of the same kind can be cascaded on the through port and independently tuned at the desired wavelength.

4. Conclusion

In this work, a novel tunable reflector based on indirectly coupled ring resonators has been presented. This device can be configured through thermal tuning and allows obtaining a single narrow-band selective mirror. An analytical model based on transfer matrices has been used to investigate the device behavior and to identify the role of the different building parameters on the maximization of the performance. Experimental results demonstrate the device functionalities. The tuned reflections (FWHM < 55 pm) in a 37 nm of wavelength range show $Q \approx 30{,}000$ and an average reflection coefficient of 0.55. The reflection strength is found to be sensitive to round trip propagation losses. However, as the analytical model suggests, higher reflectivity can be obtained by improving the fabrication quality.

The design considerations allowing to achieve a single wavelength reflection with high side mode suppression have been addressed. Unlike conventional directly coupled ring based reflectors, which require the backward coupling of counter propagating modes, the presented indirectly coupled ring topology uses forward propagation and needs only phase shift alignment of the resonators.

The proposed scheme offers more precisely tuned reflected wavelength and can be an alternative device to Distributed Bragg gratings and photonic crystals for the use as an external reflective cavity as well as an internal cavity in the integration platforms that use active materials for single wavelength laser applications, sensing schemes as well as feedback systems in scalable ring based switching architectures.

Appendix

It can be seen from the Fig. 2 that $E_2^{\pm}$, $E_3^{\pm}$ and $E_6^{\pm}$, $E_7^{\pm}$ have phase difference of $e^{i3\theta_1/4}$ and $e^{i3\theta_2/4}$, respectively. Similarly, $E_4^{\pm}$, $E_5^{\pm}$ and $E_8^{\pm}$, $E_9^{\pm}$ have one quarter of total round-trip phase shift defined as $e^{i\theta_1/4}$ and $e^{i\theta_2/4}$. The constituting equations can be written from the coupling matrices for the (+) signed amplitudes as

$$E_2^+ = (c_1 + 0.5)E_5^+ + c_2E_1^+ + (c_1 - 0.5)E_9^+ \tag{16}$$

$$E_3^+ = E_2^+ e^{i\frac{3\theta_1}{4}} \alpha_1^{\frac{3}{4}} \tag{17}$$

$$E_4^+ = E_3^+ \cos(k_1 L_{c1}) \tag{18}$$

$$E_5^+ = E_4^+ e^{i\frac{\theta_1}{4}} \alpha_1^{\frac{1}{4}} \tag{19}$$

$$E_6^+ = (c_1 - 0.5)E_5^+ + c_2E_1^+ + (c_1 + 0.5)E_9^+ \tag{20}$$

$$E_7^+ = E_6^+ e^{i\frac{3\theta_2}{4}} \alpha_2^{\frac{3}{4}} \tag{21}$$

$$E_8^+ = E_7^+ \cos(k_2 L_{c2}), \tag{22}$$

Optics EXPRESS

$$E_9^+ = E_8^+ e^{i\frac{\theta_2}{4}} \alpha_2^{\frac{1}{4}} \tag{23}$$

$$E_{10}^+ = -i * E_7^+ \sin(k_2 L_{c2}) \tag{24}$$

$$E_{11}^+ = E_{10}^+ e^{i\theta_{Ly}} \alpha_{Ly} \tag{25}$$

and the (−) signed mode amplitudes,

$$E_1^- = c_2(E_2^- + E_6^-) \tag{26}$$

$$E_2^- = E_3^- e^{i\frac{3\theta_1}{4}} \alpha_1^{\frac{3}{4}} \tag{27}$$

$$E_3^- = E_4^- \cos(k_1 L_{c1}) - i * \sin(k_1 L_{c1}) E_{11}^+ \tag{28}$$

$$E_4^- = E_5^- e^{i\frac{\theta_1}{4}} \alpha_1^{\frac{1}{4}} \tag{29}$$

$$E_5^- = (c_1 - 0.5)E_6^- + (c_1 + 0.5)E_2^- \tag{30}$$

$$E_6^- = E_7^- e^{i\frac{3\theta_2}{4}} \alpha_2^{\frac{3}{4}} \tag{31}$$

$$E_7^- = E_8^- \cos(k_2 L_{c2}) - i * \sin(k_2 L_{c2}) E_{10}^- \tag{32}$$

$$E_8^- = E_9^- e^{i\frac{\theta_2}{4}} \alpha_2^{\frac{1}{4}} \tag{33}$$

$$E_9^- = (c_1 - 0.5)E_2^- + (c_1 + 0.5)E_6^- \tag{34}$$

$$E_{10}^- = E_{11}^- e^{i\theta_{Ly}} \alpha_{Ly} \tag{35}$$

$$E_{11}^- = -i * \sin(k_1 L_{c1}) E_3^+. \tag{36}$$

According to the matrices (1), (2) and (5), the through port E_{p3}, North drop port E_{p2} and South drop port E_{p4} can be defined as followings

$$E_{p2} = E_{11}^+ \cos(k_1 L_{c1}) - i * \sin(k_1 L_{c1}) E_4^- \tag{37}$$

$$E_{p3} = c_2(E_5^+ + E_9^+) + 2c_1 E_1^+ \tag{38}$$

$$E_{p4} = E_{10}^- \cos(k_2 L_{c2}) - i * \sin(k_2 L_{c2}) E_8^-. \tag{39}$$

Starting from Eq. (16), by substituting the redefined E_5^+ and E_9^+ obtained from the Eqs. (17), (18) and (21), (22), E_2^+ can be found as

$$E_2^+ = \frac{c_2 E_1^+ + M_2^- E_6^+}{1 - M_1^+} \tag{40}$$

and by substituting the same equations to Eq. (20), one can get,

$$E_6^+ = \frac{c_2 E_1^+ + M_1^- E_2^+}{1 - M_2^+} \tag{41}$$

where $M_{(1,2)}^{\pm} = (c_{(1,2)} \pm 0.5)\cos(k_{(1,2)} L_{c_{(1,2)}}) e^{i\theta_{(1,2)}} \alpha_{(1,2)}$.

Optics EXPRESS

Finally, E_2^+ and E_6^+ can be written in terms of input port:

$$E_2^+ = \frac{E_{in} e^{i\theta_{Lx}} \alpha_{Lx} B_2 c_2}{A} \tag{42}$$

and

$$E_6^+ = \frac{E_{in} e^{i\theta_{Lx}} \alpha_{Lx} B_1 c_2}{A} \tag{43}$$

where $B_{(1,2)} = 1 - M_{(1,2)}^+ + M_{(1,2)}^-$ and $A = (1 - M_1^+)(1 - M_2^+) - M_1^- M_2^-$.

Using (42) and (43), all the other positive sign equations can be defined according to the input. Similarly negative signed E_2^- can be derived by substituting the Eqs. (28) , (29) and (30) (34), as following

$$E_2^- = \frac{E_6^- M_1^- - i * \sin(k_1 L_{c1}) e^{i3\theta_1/4} E_{11}^+}{1 - M_1^+} \tag{44}$$

whereas E_6^- can be redefined by substituting the Eqs. (32) , (33) and (34) to (31)

$$E_6^- = \frac{E_2^- M_2^- - i * \sin(k_2 L_{c2}) e^{i3\theta_2/4} E_{10}^-}{1 - M_2^+}. \tag{45}$$

Next, by substituting (45) to (44) one can get

$$E_2^- = \frac{-iE_{10}^- M_1^- \sin(k_2 L_{c2}) e^{i3\theta_2/4} - i(1 - M_2^+) \sin(k_1 L_{c1}) e^{i3\theta_1/4} E_{11}^+}{A}. \tag{46}$$

Since the E_{10}^- and E_{11}^+ are known from the previous calculations, the overall equation system can be solved with having explicit descriptions of $E_2^\pm$ and $E_6^\pm$. Therefore, the final explicit expressions of (37), (38) and (39) can be obtained.

Acknowledgments

The authors acknowledge the INPHOTEC of Sant'anna School of Advanced Technologies for the device fabrication. Gaetano Bellanca gratefully acknowledges support from "Bando per l'acquisizione di strumenti per la ricerca di Ateneo - Anno 2015" of the University of Ferrara.

Disclosures

The authors declare no conflicts of interest.

References

1. E. A. J. Marcatili, "Bends in optical dielectric guides," The Bell Syst. Tech. J. **48**(7), 2103–2132 (1969).
2. B. E. Little, J. S. Foresi, G. Steinmeyer, E. R. Thoen, S. T. Chu, H. A. Haus, E. P. Ippen, L. C. Kimerling, and W. Greene, "Ultra-compact si-sio2 microring resonator optical channel dropping filters," IEEE Photonics Technol. Lett. **10**(4), 549–551 (1998).
3. C. Manolatou, M. J. Khan, S. Fan, P. R. Villeneuve, H. A. Haus, and J. D. Joannopoulos, "Coupling of modes analysis of resonant channel add-drop filters," IEEE J. Quantum Electron. **35**(9), 1322–1331 (1999).
4. O. Schwelb, "Transmission, group delay, and dispersion in single-ring optical resonators and add/drop filters-a tutorial overview," J. Lightwave Technol. **22**(5), 1380–1394 (2004).
5. J. P. Hohimer and G. A. Vawter, "Passive mode locking of monolithic semiconductor ring lasers at 86 ghz," Appl. Phys. Lett. **63**(12), 1598–1600 (1993).
6. B. Liu, A. Shakouri, and J. E. Bowers, "Passive microring-resonator-coupled lasers," Appl. Phys. Lett. **79**(22), 3561–3563 (2001).
7. Q. Xu, B. Schmidt, S. Pradhan, and M. Lipson, "Micrometre-scale silicon electro-optic modulator," Nature **435**(7040), 325–327 (2005).
8. A. W. Poon, X. Luo, F. Xu, and H. Chen, "Cascaded microresonator-based matrix switch for silicon on-chip optical interconnection," Proc. IEEE **97**(7), 1216–1238 (2009).

Optics EXPRESS

9. F. Testa, C. J. Oton, C. Kopp, J. Lee, R. Ortu no, R. Enne, S. Tondini, G. Chiaretti, A. Bianchi, P. Pintus, M. Kim, D. Fowler, J. A. Ayúcar, M. Hofbauer, M. Mancinelli, M. Fournier, G. B. Preve, N. Zecevic, C. L. Manganelli, C. Castellan, G. Parés, O. Lemonnier, F. Gambini, P. Labeye, M. Romagnoli, L. Pavesi, H. Zimmermann, F. Di Pasquale, and S. Stracca, "Design and implementation of an integrated reconfigurable silicon photonics switch matrix in iris project," IEEE J. Sel. Top. Quantum Electron. **22**(6), 155–168 (2016).
10. N. Sherwood-Droz, H. Wang, L. Chen, B. G. Lee, A. Biberman, K. Bergman, and M. Lipson, "Optical 4×4 hitless silicon router for optical networks-on-chip (noc)," Opt. Express **16**(20), 15915–15922 (2008).
11. A. Parini, G. Bellanca, A. Annoni, F. Morichetti, A. Melloni, M. J. Strain, M. Sorel, M. Gay, C. Pareige, L. Bramerie, and M. Thual, "Ber evaluation of a passive soi wdm router," IEEE Photonics Technol. Lett. **25**(23), 2285–2288 (2013).
12. W. Bogaerts, P. De Heyn, T. Van Vaerenbergh, K. De Vos, S. Kumar Selvaraja, T. Claes, P. Dumon, P. Bienstman, D. Van Thourhout, and R. Baets, "Silicon microring resonators," Laser Photonics Rev. **6**(1), 47–73 (2012).
13. H. Sun, A. Chen, and L. R. Dalton, "A reflective microring notch filter and sensor," Opt. Express **17**(13), 10731–10737 (2009).
14. W. Shi, R. Vafaei, M. Ángel Guillén Torres, N. A. F. Jaeger, and L. Chrostowski, "Design and characterization of microring reflectors with a waveguide crossing," Opt. Lett. **35**(17), 2901–2903 (2010).
15. J. Montalvo, C. Vázquez, and D. S. Montero, "CWDM self-referencing sensor network based on ring resonators in reflective configuration," Opt. Express **14**(11), 4601–4610 (2006).
16. G. T. Paloczi, J. Scheuer, and A. Yariv, "Compact microring-based wavelength-selective inline optical reflector," IEEE Photonics Technol. Lett. **17**(2), 390–392 (2005).
17. J. Scheuer, G. T. Paloczi, and A. Yariv, "All optically tunable wavelength-selective reflector consisting of coupled polymeric microring resonators," Appl. Phys. Lett. **87**(25), 251102 (2005).
18. I. Chremmos and N. Uzunoglu, "Reflective properties of double-ring resonator system coupled to a waveguide," IEEE Photonics Technol. Lett. **17**(10), 2110–2112 (2005).
19. Y. Chung, D.-G. Kim, and N. Dagli, "Reflection properties of coupled-ring reflectors," J. Lightwave Technol. **24**(4), 1865–1874 (2006).
20. J. K. S. Poon, J. Scheuer, and A. Yariv, "Wavelength-selective reflector based on a circular array of coupled microring resonators," IEEE Photonics Technol. Lett. **16**(5), 1331–1333 (2004).
21. J. Park, T. Lee, D. Lee, S. Kim, W. Hwang, and Y. Chung, "Widely tunable coupled-ring-reflector filter based on planar polymer waveguide," IEEE Photonics Technol. Lett. **20**(12), 988–990 (2008).
22. A. Arbabi, Y. M. Kang, C.-Y. Lu, E. Chow, and L. L. Goddard, "Realization of a narrowband single wavelength microring mirror," Appl. Phys. Lett. **99**(9), 091105 (2011).
23. W. Shi, H. Yun, W. Zhang, C. Lin, T. K. Chang, Y. Wang, N. A. F. Jaeger, and L. Chrostowski, "Ultra-compact, high-q silicon microdisk reflectors," Opt. Express **20**(20), 21840–21846 (2012).
24. M. Ren, H. Cai, L. K. Chin, K. Radhakrishnan, Y. Gu, G.-Q. Lo, D. L. Kwong, and A. Q. Liu, "Coupled-ring reflector in an external-cavity tunable laser," Optica **2**(11), 940–943 (2015).
25. R. Boeck, M. Caverley, L. Chrostowski, and N. A. F. Jaeger, "Grating-assisted silicon-on-insulator racetrack resonator reflector," Opt. Express **23**(20), 25509–25522 (2015).
26. O. Schwelb and I. Frigyes, "Vernier operation of series-coupled optical microring resonator filters," Microw. Opt. Technol. Lett. **39**(4), 257–261 (2003).
27. B. E. Little, S. T. Chu, H. A. Haus, J. Foresi, and J. Laine, "Microring resonator channel dropping filters," J. Lightwave Technol. **15**(6), 998–1005 (1997).
28. C. L. Manganelli, P. Pintus, F. Gambini, D. Fowler, M. Fournier, S. Faralli, C. Kopp, and C. J. Oton, "Large-fsr thermally tunable double-ring filters for wdm applications in silicon photonics," IEEE Photonics J. **9**(1), 1–10 (2017).
29. F. Morichetti, C. Ferrari, A. Canciamilla, and A. Melloni, "The first decade of coupled resonator optical waveguides: bringing slow light to applications," Laser Photonics Rev. **6**(1), 74–96 (2012).
30. Y. Chung, D.-G. Kim, and N. Dagli, "Widely tunable coupled-ring reflector laser diode," IEEE Photonics Technol. Lett. **17**(9), 1773–1775 (2005).
31. T. Yen and Y. Hung, "Narrowband dual-wavelength silicon waveguide Bragg reflectors," J. Lightwave Technol. **37**(20), 5326–5332 (2019).
32. F. Morichetti, A. Canciamilla, M. Martinelli, A. Samarelli, R. M. De La Rue, M. Sorel, and A. Melloni, "Coherent backscattering in optical microring resonators," Appl. Phys. Lett. **96**(8), 081112 (2010).
33. COMSOL Multiphysics, https://www.comsol.com.
34. Lumerical FDTD, https://www.lumerical.com.
35. P. Pintus, C. Manganelli, S. Tondini, M. Mancinelli, F. Gambini, C. Castellan, F. Di Pasquale, L. Pavesi, F. Testa, and C. J. Oton, "Silicon photonic toolkit for integrated switching matrices," in *18th Italian National Conference on Photonic Technologies (Fotonica 2016)*, (2016), pp. 1–4.
36. A. Yariv, "Coupled-mode theory for guided-wave optics," IEEE J. Quantum Electron. **9**(9), 919–933 (1973).
37. H. Kogelnik and R. Schmidt, "Switched directional couplers with alternating $\Delta\beta$," IEEE J. Quantum Electron. **12**(7), 396–401 (1976).
38. A. Takagi, K. Jinguji, and M. Kawachi, "Wavelength characteristics of (2*2) optical channel-type directional couplers with symmetric or nonsymmetric coupling structures," J. Lightwave Technol. **10**(6), 735–746 (1992).

Optics EXPRESS

39. C.-M. Kim and Y.-J. Im, "Switching operations of three-waveguide optical switches," IEEE J. Sel. Top. Quantum Electron. **6**(1), 170–174 (2000).
40. A. Yariv, "Universal relations for coupling of optical power between microresonators and dielectric waveguides," Electron. Lett. **36**(4), 321–322 (2000).
41. A. Yariv, "Critical coupling and its control in optical waveguide-ring resonator systems," IEEE Photonics Technol. Lett. **14**(4), 483–485 (2002).
42. M. Milanizadeh, D. Aguiar, A. Melloni, and F. Morichetti, "Canceling thermal cross-talk effects in photonic integrated circuits," J. Lightwave Technol. **37**(4), 1325–1332 (2019).